

Nonlinear Saturation of Ballooning Modes in Stellarators

X. Chu^{1,2}, S. C. Cowley^{1,2}, N. Ferraro¹, Y. Zhou³, F. I. Parra^{1,2}

¹Princeton Plasma Physics Laboratory, 100 Stellarator Road, Princeton, NJ 08540, USA

²Princeton University, Princeton, NJ 08544, USA

³School of Physics and Astronomy, Institute of Natural Sciences, and MOE-LSC, Shanghai Jiao Tong University, Shanghai 200240, China

E-mail: xchu@pppl.gov

ORCID IDs:

Xu Chu: <https://orcid.org/0000-0002-0382-6428>

July 2023

Abstract

Ballooning mode saturation is investigated in realistic stellarator configurations using the flux tube approach of Ham et. al. [1] [2]. The method is adapted to account for the lack of exact force balance in stellarator equilibrium solvers that assume existence of nested flux surfaces. A variational approach for calculating flux tube energy is developed to overcome this force error problem in stellarator numerical equilibria. Saturated (equilibrium) flux tube states that cross 10-20% of the plasma minor radius are shown to exist for linearly ballooning unstable profiles. It is shown that several features of the displaced flux tube structure in a full nonlinear MHD simulation of Wendelstein 7X are reproduced by our model. Saturated states are found in a compact stellarator equilibrium close but below the marginal ballooning linear instability, i.e. the unperturbed equilibrium is metastable. This suggests that Edge-Localized-Mode-like explosive MHD behavior may be possible in stellarators.

Keywords— Ballooning Mode, Nonlinear, Saturation, Stellarator

1. Introduction

Stellarators usually have better MHD stability properties than tokamaks due to their small net toroidal current. High β operation with average β from 3% to 5% has been demonstrated in various devices such as W7AS [3], LHD [4] and W7X [5]. In contrast to tokamaks, where linear MHD stability analysis predicts well the β limits, stellarators can sometimes operate beyond usual linear stability boundary like the Mercier interchange limit [6], or the ideal ballooning limit [6]. In these cases, magnetic fluctuations are observed after β exceeds these linear stability limits, but their amplitude remains small and they merely lead to an increase in transport without total loss of confinement. This is known as a soft β limit, in opposition to hard β limits. Hard β limits are characterized by events that end in bursty transport with large heat flux to the plasma facing components, usually intolerable in reactor conditions. Exmaples of hard beta limits are disruptions and Edge Localized Modes (ELMs) [7] in tokamaks. We need to understand which configurations have soft or hard beta limits in stellarators, motivating the use of nonlinear MHD models. Hard limits can be particularly dangerous for future stellarator power plants where the stored energy is much higher than in stellarators today.

In this paper we focus on the nonlinear behavior of ideal ballooning mode. Baloooning modes are high-mode-number pressure-driven ideal MHD instabilities that extend along magnetic field lines [8]. They can lead to both soft and hard β limits. An example of hard β limit related to ballooning modes is ELMs in tokamaks. In stellarators, MHD phenomena resembling ballooning modes has been observed during high β operation of W7AS [9]. In addition, a ballooning mode is suspected to be responsible for core density collapse in LHD [10].

The linear behavior of ballooning modes has been studied extensively in tokamaks [11] [12] and stellarators [13] [14], both analytically and numerically [15] [16] [17]. For the nonlinear behavior of ballooning modes, theory has been developed for the early nonlinear stage [18] [19] [20] and the intermediate nonlinear stage [21] when explosive growth of ballooning modes forms isolated plasma ‘fingers’. A model for the nonlinear saturated stage of ballooning modes has predicted that certain tokamak configurations are metastable to ballooning modes [1] [2].

With the advances in extended MHD codes such as M3D-C1, JOREK and NIMROD, the nonlinear behavior of ballooning modes can be studied numerically. The recent extension of M3D-C1 to stellarator geometries [22] has enabled the study of W7X high beta configurations

near the ideal ballooning limit where benign saturation is observed [23].

In this work, we study the nonlinear saturation of ballooning modes in stellarators by implementing the flux tube model described in [1] in realistic stellarator numerical equilibria obtained with the DESC equilibrium solver [24]. We show that saturation levels can be calculated and that metastable stellarator equilibria exist. These metastable equilibria might explain ELM-like behavior that has been observed in stellarators [3].

The paper is organized as follows. In Section 2, the flux tube model for ballooning modes developed in [1] is reviewed and the numerical implementation in real stellarator geometries is presented. In Section 3, saturated ballooning modes are qualitatively described. Convergence analysis and benchmarks are presented. The model is then compared with the flux tube structure observed in a recent M3DC1 simulation for W7X [23] in the nonlinear saturation stage. The assumptions used in the model are tested and the flux tube shape in the simulation is compared with the model, showing good agreement. In Section 4, energy release is calculated. In Section 5, a case study of a compact QA(Quasi-axisymmetric) equilibrium [25] near ideal ballooning marginal stability is presented and the existence of metastable equilibria is demonstrated. In Section 6, we discuss the applicability of the model and how connections might be drawn to soft/hard β limits in stellarators.

2. Flux Tube Model and Numerical Implementation

In this section we revisit the model in [1], and apply it to general 3D configurations.

We consider a perturbed state of the equilibrium, with a field line aligned flux tube displaced from its original position, as shown in Fig.1. The flux tube is thin and elongated in the direction of its movement, [1] so that the change of the background magnetic field remains unimportant as the flux tube slides along a surface that is everywhere tangential to the background magnetic field. We call such a surface an α **surface** - see Eq. (2) and the discussion below for more details. By moving along an α surface, the perturbed flux tube does not cross any background magnetic field lines, i.e. the topology of the field lines does not change. The background field lines simply part to allow the perturbed flux tube to pass.

The magnetic field and pressure inside the flux tube are denoted \mathbf{B}_{in} and p_{in} , respectively. Just outside the tube, the magnetic field and the pressure are \mathbf{B}_{out} and p_{out} .

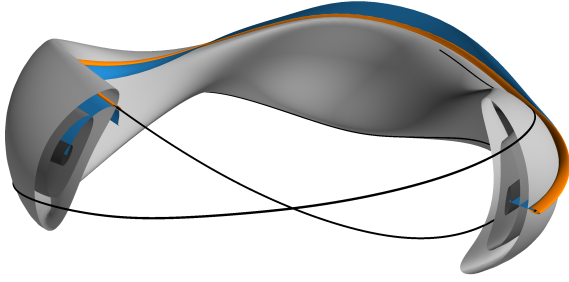


Figure 1: An illustration of the geometry of the flux tube model using a compact QA [25] equilibrium. Flux surfaces are plotted in grey. The surface of constant α , which is tangential to the equilibrium field at all points, is depicted in blue. The perturbed flux tube (orange color) moves on the α surface with its elliptical cross-section elongated along the α surface. A field line inside the flux tube is plotted in black – note that it is bent with respect to the equilibrium field. We assume that the flux tube does not intersect itself after going around the device.

We assume the flux tube is sufficiently narrow that it does not perturb the magnetic field nor the pressure outside the tube. Thus,

$$\mathbf{B}_{out} = \mathbf{B}_0 = \nabla\psi \times \nabla\alpha_0, \quad p_{out} = p_0(\psi), \quad (1)$$

where \mathbf{B}_0 is the original equilibrium field, $p_0(\psi)$ is the equilibrium pressure profile and ψ is the toroidal magnetic flux divided by 2π . The quantity $\alpha_0 = \theta - \iota\zeta$ is the nonperiodic Clebsch coordinate, where ζ is an arbitrary toroidal angle, θ is a corresponding straight field line poloidal angle, and $\iota = \iota(\psi)$ is the rotational transform. Since DESC [24] is used for equilibrium calculation, ζ from here on should be understood as the toroidal angle in cylindrical coordinates. However, the theory can be applied to any general toroidal angle without any modifications.

Since $\mathbf{B}_0 \cdot \nabla\alpha_0 = \mathbf{B}_0 \cdot \nabla\psi = 0$, a general surface that is everywhere tangent to the background equilibrium magnetic field can be written as

$$\alpha = \alpha_0 - f(\psi) = 0, \quad (2)$$

where the flux function $f(\psi)$ is undetermined to the order that we perform these calculation. We refer to the surface determined by Eq. (2) as α **surface** from here on. Note that $\mathbf{B}_0 = \nabla\psi \times \nabla\alpha$ for all $f(\psi)$. Choosing an α surface is equivalent to choosing $f(\psi)$. The alpha surface intersects itself on rational surfaces when traced around the machine one or more times. However, we assume that the perturbed flux tube does not intersect itself where the perturbation is significant. In such cases, we can locate points on the alpha surface by using the coordinates of ψ and ζ .

The tangent space of the α surface is spanned by \mathbf{b}_0 and \mathbf{e}_\perp , where $\mathbf{b}_0 = \mathbf{B}_0/|\mathbf{B}_0|$ is a unit vector in the direction of the background magnetic field, and \mathbf{e}_\perp is a vector perpendicular to \mathbf{b}_0 and $\nabla\alpha$,

$$\mathbf{e}_\perp = \nabla\alpha \times \mathbf{b}_0. \quad (3)$$

All equilibrium quantities (e.g. $\mathbf{e}_\perp, \mathbf{b}_0, \nabla\alpha, B_0$) are known on the alpha surface as functions of ψ and ζ . To simplify our notation, the α dependence is not made explicit for the rest of this paper.

The perturbed flux tube has a width δ_α in the $\nabla\alpha$ direction, and a width of δ_\perp along the α surface in the \mathbf{e}_\perp direction. We assume $\delta_\alpha \ll \delta_\perp \ll L$ where L is the typical equilibrium scale – for a more detailed discussion of the limit of validity of this flux tube model, see [1]. Each field line inside the flux tube stays on the alpha surface (to leading order in $\delta_\alpha/L \ll 1$) and is represented by its radial (ψ) displacement (with respect to its initial location) η as a function of the position along the line, given by the toroidal angle ζ ,

$$\psi = \psi_0 + \eta(\zeta, \psi_0) \quad (4)$$

Here, ψ_0 is the flux surface label where the field line originally locates. We assume that the field lines inside the tube are bent with a radius of curvature of the order of the equilibrium length scale; thus $\partial\eta/\partial\zeta \sim \mathcal{O}(\psi_{edge})$, where ψ_{edge} is the value of normalized toroidal flux ψ at the edge of the stellarator. Since the magnetic field inside the flux tube is tangent to the α surface, it can be represented as

$$\mathbf{B}_{in}(\zeta, \psi_0) = B_\parallel(\zeta, \psi_0)\mathbf{B}_0(\psi, \zeta) + B_\perp(\zeta, \psi_0)\mathbf{e}_\perp(\psi, \zeta). \quad (5)$$

Note that \mathbf{B}_0 and \mathbf{e}_\perp are evaluated at the perturbed location $\psi = \psi_0 + \eta(\zeta)$ on the α surface. We can relate B_\perp to η and its derivative,

$$\left. \frac{d\eta}{d\zeta} \right|_{\psi_0} = \frac{\mathbf{B}_{in} \cdot \nabla\psi}{\mathbf{B}_{in} \cdot \nabla\zeta} = \frac{B_\perp \mathbf{e}_\perp \cdot \nabla\psi}{B_\parallel \mathbf{B}_0 \cdot \nabla\zeta + B_\perp \mathbf{e}_\perp \cdot \nabla\zeta}. \quad (6)$$

The equilibrium state of the flux tube is obtained from MHD force balance [1]. From parallel force balance ($\mathbf{B}_{in} \cdot \nabla p_{in} = 0$), we find that hydrodynamic pressure is constant to lowest order along the perturbed field line. Since the perturbed flux tube connects to the initial surface ψ_0 at $\zeta \rightarrow \infty$, $p_{in} = p_0(\psi_0)$. The smallest spatial scale of the flux tube, δ_α , is in the α direction. In the perpendicular force balance in that direction, the magnetic field line tension can be neglected to leading order compared to the total pressure ($p + B^2/(2\mu_0)$) gradient, where μ_0 is the vacuum permittivity. As a result, $B_{in} = |\mathbf{B}_{in}|$ is known as a function of spacial coordinates alone,

$$\begin{aligned} B_{in}^2 &= B_{out}^2 + 2\mu_0(p_{out} - p_{in}) \\ &= B_0^2(\psi, \zeta) + 2\mu_0(p_0(\psi) - p_0(\psi_0)), \end{aligned} \quad (7)$$

where $B_{out} = B_0(\psi, \zeta)$ and $p_{out} = p_0(\psi)$ are evaluated at the perturbed location of the flux tube. We can therefore relate B_\parallel to B_\perp as

$$B_\parallel = \sqrt{1 + 2\mu_0\Delta p/B_0^2 - |\mathbf{e}_\perp|^2 B_\perp^2/B_0^2}, \quad (8)$$

where $\Delta p = p_0(\psi) - p_0(\psi_0)$.

Using the results above and force balance in the \mathbf{e}_\perp direction, we have an equation for η . Using Eq. (7) and the background magnetic field force balance $\mathbf{B}_0 \cdot \nabla\mathbf{B}_0 - \nabla(p_0 + B_0^2/2\mu_0) = 0$, and imposing that the force along \mathbf{e}_\perp

on the perturbed flux tube vanishes give the generalised Archimedes principle equation

$$\mu_0 F_{\perp} = (\mathbf{B}_{in} \cdot \nabla \mathbf{B}_{in} - \mathbf{B}_0 \cdot \nabla \mathbf{B}_0) \cdot \mathbf{e}_{\perp} = 0. \quad (9)$$

Using the representation of the \mathbf{B}_{in} in Eq. ((5)), this equation can be expanded as

$$\begin{aligned} \mathbf{B}_{in} \cdot \nabla (|\mathbf{e}_{\perp}|^2 B_{\perp}) + (B_{\parallel}^2 - 1) B_0^2 \boldsymbol{\kappa} \cdot \mathbf{e}_{\perp} \\ + B_{\perp} B_{\parallel} (\mathbf{e}_{\perp} \cdot \nabla \mathbf{B}_0) \cdot \mathbf{e}_{\perp} - B_{\perp} (\mathbf{B}_{in} \cdot \nabla \mathbf{e}_{\perp}) \cdot \mathbf{e}_{\perp} = 0. \end{aligned} \quad (10)$$

Note that we have the following equalities

$$\begin{aligned} (\mathbf{e}_{\perp} \cdot \nabla \mathbf{b}_0) \cdot \mathbf{e}_{\perp} &= -\mathbf{b}_0 \cdot \nabla |\mathbf{e}_{\perp}|^2 / 2 + [\mathbf{e}_{\perp} \times (\nabla \times \mathbf{e}_{\perp})] \cdot \mathbf{b}_0 \\ &= \mathbf{b}_0 \cdot \nabla |\mathbf{e}_{\perp}|^2 / 2 - |\mathbf{e}_{\perp}|^2 \mathbf{b}_0 \cdot \nabla B_0 / B_0. \end{aligned} \quad (11)$$

Here, the definition $\mathbf{e}_{\perp} = \nabla \alpha \times \mathbf{b}_0$, $\mathbf{b}_0 \cdot \nabla \alpha = 0$, $|\mathbf{e}_{\perp}|^2 = |\nabla \alpha|^2$ and $\nabla \cdot \mathbf{B}_0 = 0$ are utilized to simplified the second term on the RHS of the first equality. Substituting Eq. (11) into Eq. (10), we derive the nonlinear ballooning equation

$$\begin{aligned} \mathbf{B}_{in} \cdot \nabla \left(\frac{|\mathbf{e}_{\perp}|^2}{B_0} B_{\perp} \right) + (B_{\parallel}^2 - 1) B_0 \boldsymbol{\kappa} \cdot \mathbf{e}_{\perp} \\ - B_{\perp}^2 B_0 \mathbf{e}_{\perp} \cdot \nabla \left(\frac{|\mathbf{e}_{\perp}|^2}{2B_0^2} \right) = 0. \end{aligned} \quad (12)$$

where $\boldsymbol{\kappa} = \mathbf{b}_0 \cdot \nabla \mathbf{b}_0$ is the background magnetic field curvature. For convenience, we introduce another variable Y ,

$$Y(\zeta, \psi_0) = \frac{|\mathbf{e}_{\perp}|^2}{B_0} B_{\perp}. \quad (13)$$

We note that $\mathbf{B}_{in} \cdot \nabla Y = (\mathbf{B}_{in} \cdot \nabla \zeta) \frac{dY}{d\zeta} \Big|_{\psi_0}$. Thus,

$$\begin{aligned} \frac{dY}{d\zeta} \Big|_{\psi_0} &= \frac{B_0}{B_{\parallel} \mathbf{B}_0 \cdot \nabla \zeta + B_{\perp} \mathbf{e}_{\perp} \cdot \nabla \zeta} \left[B_{\perp}^2 \mathbf{e}_{\perp} \cdot \nabla \left(\frac{|\mathbf{e}_{\perp}|^2}{2B_0^2} \right) \right. \\ &\quad \left. - (B_{\parallel}^2 - 1) \boldsymbol{\kappa} \cdot \mathbf{e}_{\perp} \right]. \end{aligned} \quad (14)$$

Eqs. (6) and (14) along with the algebraic relations Eqs. (8) and (13) constitute two coupled first-order nonlinear ordinary differential equations for $\eta(\zeta, \psi_0)$ and $Y(\zeta, \psi_0)$. The right hand side of Eqs. (6) and (14) can be evaluated algebraically given the background MHD equilibrium, η , Y and the α surface. Note that ψ_0 is a parameter in these equations and thus each field line in the flux tube can be solved independently. In this paper we assume that the tube is small enough that one field line is representative of the motion of the whole flux tube and we do not attempt to solve for the structure inside the tube.

We seek solutions of Eqs. (6) and (14) with $\eta \rightarrow 0$ and $Y \rightarrow 0$ as $\zeta \rightarrow \pm\infty$. The solution for a chosen ψ_0 can in principle be found via a shooting method. We chose a simulation domain extended along the field line, given by $\zeta \in [\zeta_0, \zeta_1]$, where ζ_0 and ζ_1 are large numbers, usually encompassing six or more toroidal turns. At ζ_0 , we impose zero displacement and we provide a guess Y_0 for the value of Y . Eqs. (6) and (14) are then integrated numerically to obtain $Y(\zeta, \psi_0)$ and $\eta(\zeta, \psi_0)$ for $\zeta \in [\zeta_0, \zeta_1]$. In general,

for any given guess Y_0 , η does not go to zero at ζ_1 , but for some equilibria and particular nonzero discrete values of the amplitude Y_0 , the numerical solution satisfies the boundary condition $\eta(\zeta_1) = 0$. If such nonzero values of Y_0 exist then these are valid saturated flux tube states. We use the brentq root finding algorithm [26] to obtain these nonzero values of Y_0 . First, a set of solutions of Eq. (12) is generated using different values of Y_0 . We use this scan to determine the intervals in Y_0 that contain zero displacement solutions at the right boundary ζ_1 . The interval information is then passed to the brentq algorithm to find the accurate Y_0 value that satisfies the boundary condition.

We have obtained the solution for η for large values of ζ (Appendix C). This analytical solution is not used to prescribe the boundary conditions for the shooting method because the derivation assumes that the solution extends sufficiently far along the magnetic field line that it samples a significant portion of the flux surface ψ_0 . This would require extremely long simulation domains.

In [27], an energy functional for saturated flux tubes was derived. It is the total magnetic energy in a flux tube per unit magnetic flux,

$$\mathcal{E} = \lim_{x \rightarrow \infty} \left(\int_{-x}^x \mathbf{B}_{in} \cdot d\mathbf{r} - \int_{-x}^x \mathbf{B}_0 \cdot d\mathbf{r}_0 \right), \quad (15)$$

where the first functional integral is taken along a perturbed field line (\mathbf{B}_{in}) on the α surface, with the field strength B_{in} given by Eq. (7), and the second integral in Eq. (15) is along the unperturbed field line. Flux tube equilibrium solutions to Eqs. (6) and (14) are stationary field line paths of the functional (*i.e.* paths for which the functional derivative vanishes, $\delta\mathcal{E}/\delta\mathbf{r} = 0$). Stable flux tube equilibria are (local or global) minima of \mathcal{E} .

In Appendix B, a variational derivation of Eq. (12) from the energy functional (15) is given. It is worth noting that this derivation requires the assumption of equilibrium force balance. It turns out that in a numerical equilibrium where only approximate force balance is achieved, the compatibility of this energy functional with the flux tube saturation equation is not guaranteed. We will discuss this more in the following sections.

The set of ODEs in Eqs. (6) and (14) is implemented using MHD equilibrium solutions of the DESC equilibrium solver [24]. First, an α surface is selected by choosing f in $\alpha = \theta - \iota\zeta - f(\psi) = 0$. Then, a 2D field line aligned grid is generated on the chosen α surface. This grid is uniform in $\rho - \rho_0$ and ζ . Here the flux surface label, $\rho = \rho(\psi)$, is the square root of the normalized toroidal flux, and $\rho_0 = \rho(\psi_0)$ is the flux surface label of the unperturbed flux tube. Equilibrium-related quantities needed for evaluating the right-hand side of the ODEs are calculated on the grid and interpolated. Saturated flux tubes are calculated using the shooting method described above. The detailed implementation based on DESC is outlined in Appendix A.

For the boundary condition to work, the perturbed flux tube must asymptotically approach the unperturbed flux tube for large ζ . This requires $\eta \sim \zeta^{\nu}$ with $\nu < -1$ as $\zeta \rightarrow \infty$ because the displacement in poloidal angle is $\Delta\theta = \iota(\psi_0 + \eta(\zeta))\zeta + f(\psi_0 + \eta(\zeta)) \approx \zeta \iota' \eta(\zeta) \sim \zeta^{\nu+1}$ due to finite magnetic shear ι' . A displacement $\eta \sim \zeta^{\nu}$

with $\nu \geq -1$ would cause a poloidal displacement $\Delta\theta$ with respect to the original field line that does not decrease as ζ increases. The multi-scale asymptotic expansion performed in Appendix C predicts the value of ν . The exponent ν is the same as the one obtained from the Mercier analysis of the linear ballooning equation as long as $\nu < -1$. Therefore, the calculation is limited to $\nu_{\text{Mercier}} < -1$. For $\nu \geq -1$, the analysis in Appendix C is no longer valid because the displaced flux tube does not tend towards the original flux tube for large ζ . We have found that, for $\nu \geq -1$, numerical solutions to the nonlinear ballooning ODE with zero displacement at the simulation boundary can still be found. However, they intersect the original field line at a finite slope and tend to balloon further radially outwards if the numerical domain is extended, that is, for cases with $\nu \geq -1$, the solutions for the displaced flux tube do not converge with simulation domain size.

3. Flux Tube Saturated States and Comparison with M3D-C1

In this section, we first show typical numerical solutions to the nonlinear ballooning equation 12 in general stellarator geometry. We also benchmark the code with linear ballooning stability calculations. Then, we compare the model with nonlinear MHD simulations. We confirm key assumptions of our model by examining a nonlinear M3D-C1 simulation of a W7-X configuration that has benign saturation of ballooning modes [23], and we compare the flux tube shape provided by our model to the flux tube states extracted from that simulation.

3.1. Calculation of Flux Tube Saturated States

In Fig. 2, examples of the shape of saturated flux tube states are shown. In this figure, we plot the change in normalized minor radius $\Delta\rho = \rho(\zeta) - \rho_0$ as a function of ζ . There is a discrete number of saturated flux tubes on a given α surface, each corresponding to a stationary point in the energy curve. In this particular case, there are two different nonlinear solutions (other than the unperturbed state), and the flux tube with the largest displacement is stable, whereas the other flux tube is unstable. The stability is determined by the energy dependence on the displacement. The stable flux tube is at a local energy minimum and the unstable at a local maximum. We do not show the energy map here. It will be discussed in detail in section 4. The flux tube deforms radially outwards in the region with bad curvature as in the linear ballooning mode calculation. In fact, the shape of the nonlinear saturated flux tube qualitatively resemble the linear ballooning eigenmode shape.

The convergence of the flux tube shape has been checked, with respect to solution domain size, interpolation resolution, ODE solving tolerance and root finding tolerance for the shooting method. As shown in the Fig. 2, curves obtained with different resolutions overlap. For the base case, 500 ζ grid points for $\zeta \in [-12\pi, 12\pi]$ and 41 $\Delta\rho$ grid points for $\Delta\rho \in [-0.1, 0.2]$ are used. A relative tolerance of 1×10^{-6} and an absolute tolerance of 1×10^{-7}

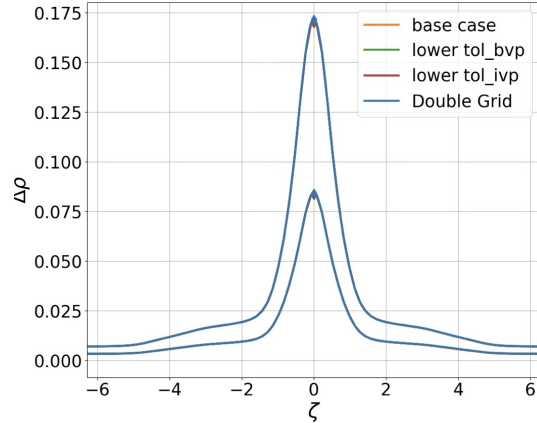


Figure 2: Typical shape of the saturated flux tube states, plotted as radial displacement in normalized minor radius $\Delta\rho$ v.s. cylindrical toroidal angles. This case is calculated on a compact QA [25] equilibrium on a stellarator symmetric α surface in the domain $\zeta \in [-12\pi, 12\pi]$. Two saturated states are presented, each corresponding to a stationary point of the energy curve. The procedure for generating such energy curve will be presented in section 4. Four solutions of different resolutions are plotted for each saturated state, showing good convergence.

are used for the RK45 ODE solver. An absolute tolerance of 2×10^{-12} and relative tolerance of 1×10^{-14} are used for the root finding algorithm. For the "lower tol_bvp" case, the absolute tolerance of the root finder is improved to 2×10^{-14} . For the "lower tol_ivp" case, the relative tolerance and the absolute tolerance of the RK45 ODE solver are improved to 1×10^{-10} and 1×10^{-11} , respectively. For the double grid case, the grid points in the ζ direction are increased to 1000.

The nonlinear solver is benchmarked against linear ballooning results from COBRAVMEC. This benchmark is performed by adding the linear inertia term $min_i \Delta\rho \omega^2 |e_\perp|^2 / B_0^2$ on the RHS of Eq. (12). Then Eq.12 is solved with a very small slope starting at one end of the grid, and ω^2 is adjusted in the shooting method solver to have the solution cross zero at the other side of the domain. The calculated growth rate is compared with COBRAVMEC in Fig. (3), showing good agreement as the initial slope is decreased.

3.2. Comparison with Nonlinear MHD Simulation

To verify the assumptions used in the derivation of this flux tube model and check the accuracy of its prediction, we proceed to compare our model to a recent ideal MHD M3D-C1 simulation of W7X where benign saturation of ballooning modes is observed [23]. We show that the flux tube structures studied in this paper are indeed present in the nonlinear saturation stage of the simulation. We

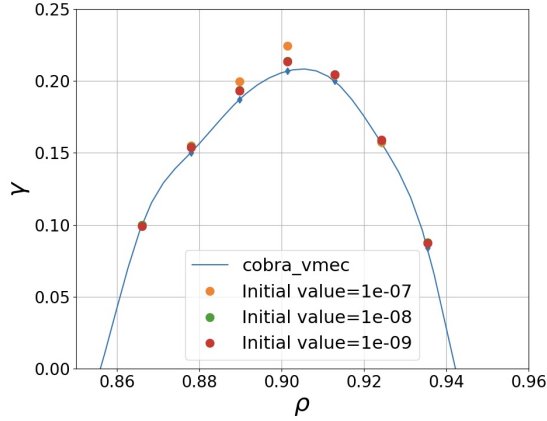


Figure 3: Benchmark against COBRAVMEC. Here, ρ is normalized minor radius and γ is linear ballooning growth rate normalized to the Alfvén time. The growth rates calculated from our nonlinear model with small initial condition are shown with solid dots. The initial values Y have the unit of meters⁻¹

check the assumptions made in the theory against the flux tube structure in the simulation, and we find that the assumptions are justified. As a result, the flux tube shape that we calculate are also in good agreement with the flux tube structure extracted from the simulation.

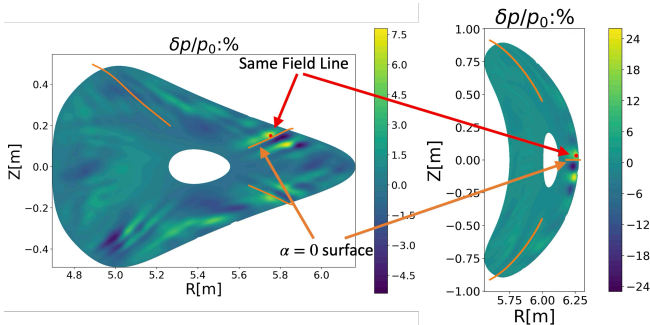


Figure 4: Pressure perturbation on the $\zeta = \pi/5$ (left subfigure) and $\zeta = 0$ (right subfigure) cross sections at $t = 2500\tau_A$ of the M3D-C1 simulation reported in [23]. Red solid circles are the intersection of the same field line with the cross sections. The three orange lines are the α surfaces $\theta - \nu\zeta = -2\pi/5, 0, 2\pi/5$.

We examine the time slice $2500\tau_A$ of the two cross sections at $\zeta = 0, \pi/5$ of the EIM 5.4% β case in [23], where ballooning modes have saturated. Here $\tau_A = 0.46\mu s$ is the Alfvén time, for a reference length of $1m$, a reference magnetic field of $1T$ and a reference density (hydrogen plasmas) of $10^{20}m^{-3}$. The perturbed pressure δp is plotted in Fig. 4. Here $\delta p = p - p_0$ with p_0 obtained from the initial VMEC equilibrium and p obtained from M3D-C1 simulation of $t = 2500\tau_A$. There are localized peaks of pressure perturbation near the edge of the simulation which

resemble the saturated flux tube structures that we are studying. We trace the magnetic field starting at the local maximum of pressure perturbation at $\zeta = 0$, indicated by the red dot in the right sub-figure. The same magnetic field line goes through the region of maximum pressure perturbation at $\zeta = \pi/5$, as show in the left sub-figure. This confirms that the localized peaks of pressure perturbation are a single flux tube extended toroidally. At $\zeta = \pi/5$, the localized structure of the pressure perturbation appears to be elongated radially. This is consistent with our assumption of a flux tube elongated along an α surface. The intersections of $\theta - \nu\zeta = 0, -2\pi/5, 2\pi/5$ surfaces with the two toroidal cross sections are indicated by the orange curves, and they indeed follow the direction of the elongated structure in the pressure perturbation.

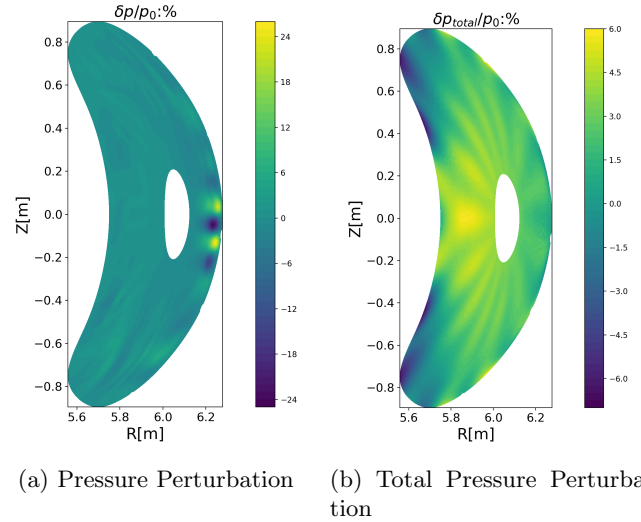


Figure 5: Comparison of relative pressure perturbation $\delta p/p_0$ and relative total pressure perturbation $\delta p_{total}/p_0$, at $\zeta = 0, t = 2500\tau_A$. Notice that the small scale structures in $\delta p/p_0$ are not present in $\delta p_{total}/p_0$, justifying the assumption of total pressure continuity in our model.

To further confirm that the observed structure is indeed the saturated flux tube, we examine two important properties of our model. The first is the continuity of total magnetic pressure $p_{total} = p + B^2/2\mu_0$ in the perpendicular direction of the flux tube. As shown in Fig. 5, the normalized total pressure perturbation $\delta p_{total}/p_0$ do not have the same small scale variations observed in the pressure perturbation $\delta p/p_0$ on the outboard side. Here $\delta p_{total} = p_{total} - p_{total0}$, where p_{total0} is obtained from the initial VMEC equilibrium, and p_{total} is obtained from M3D-C1 simulation of $t = 2500\tau_A$. Therefore, we conclude that $\partial_\alpha p_{total} = 0$ is a good approximation. The second property we check is that the pressure is constant inside the displaced flux tube. In Fig. 6, the pressure inside the flux tube p_{in} is compared with the pressure outside p_{out} . Here p_{in} is the pressure on the field line traced out in the saturated stage of the simulation, starting at a local maximum of pressure perturbation, and p_{out} is the pressure outside the

flux tube. It is obtained by evaluating the pressure of the **initial** VMEC equilibrium at the location of the flux tube. It represents the average pressure on that magnetic surface. Compared with the magnitude of variation of p_{out} along the flux tube, the magnitude of the p_{in} variation is about a factor of 6 smaller. This means that assuming constant p_{in} along the flux tube is a good approximation.

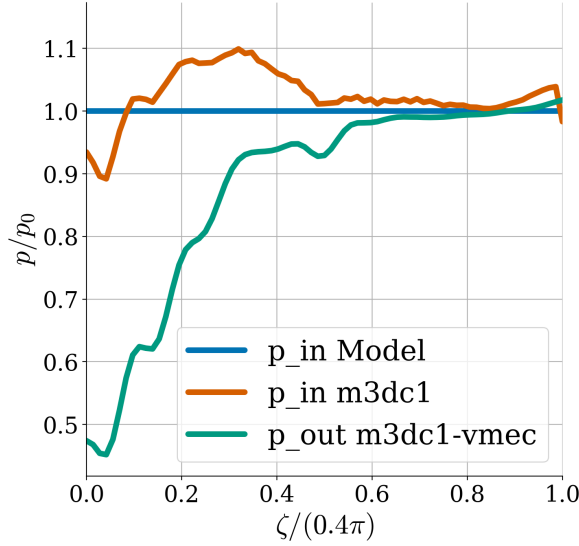


Figure 6: The pressure inside the flux tube is compared with pressure outside the flux tube. Here p_{in} denotes the value of pressure in the simulation on the field line traced from the maximum of δp at $\zeta = 0$. The quantity p_{out} is the pressure in the VMEC equilibrium along the same field line. In our model, p_{in} is assumed to be constant and equal to the pressure at long distances along the flux tube, as indicated by the blue line.

With all the above observations, we conclude that the localized pressure perturbations observed in the simulation are likely to be saturated ballooning flux tube states like the ones we discuss in this paper. To allow quantitative comparisons of the simulation with the nonlinear ballooning saturation theory, we construct a DESC equilibrium from the M3D-C1 results at $t = 2500\tau_A$. The new pressure profile is obtained by surface averaging the pressure in M3D-C1 on the surfaces of the initial VMEC equilibrium. As shown in Fig. 7, the pressure gradient has a slight flattening compared to the initial pressure gradient. A new reconstructed DESC equilibrium is obtained with this new pressure profile and zero net toroidal current.

In Fig. 8, we compare the flux tube shape extracted from the M3D-C1 simulation by following the magnetic field line at the maximum of δp in $\zeta = 0$ with the one calculated using the nonlinear ballooning equations Eq. (6) and Eq. (14). The flux surface that the unperturbed flux tube resides in, ρ_0 , is prescribed so that the pressure on that surface equals the pressure on the flux tube extracted from the simulation at $\zeta = 2\pi/5$, where p_{in} and p_{out} are the same (see the blue line in Fig. 8). The α surface is set to be $\theta - \iota\zeta = 0$, which is justified by the alignment of

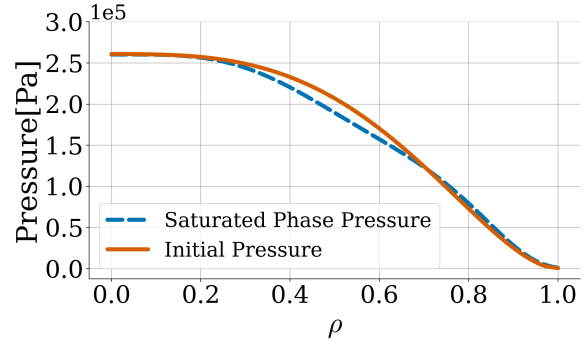


Figure 7: Average pressure profile at the saturated stage of the simulation and the initial pressure profile.

$\theta - \iota\zeta = 0$ surface with the pressure perturbation contour in the simulation. The slope of the flux tube $d\eta/d\zeta$ in the model is set to zero at $\zeta = 0$ given the stellarator symmetry of the configuration. As shown in Fig. 8, the agreement between the flux tube shape extracted from the simulation and the flux tube calculated using our model is reasonable. There is good agreement in $\zeta \in (0, \pi/5)$. The agreement is worse for $\zeta > \pi/5$, which leads to a discrepancy in the saturation level. Since the flux tube has been obtained by choosing the value of $d\eta/d\zeta$ and η at $\zeta = 0$ similar to the ones extracted from M3D-C1 instead of using the shooting method described in section 2, the flux tube intersects the unperturbed flux tube at finite length along the flux tube, and at those locations the slopes are discontinuous. The slope discontinuity is such that the tension of the magnetic field pulls the point radially outwards, as demonstrated by the arrows in Fig. 8. As a result, we would have expected the flux tube to balloon outward further. In the simulation, zero radial displacement is imposed at the boundary, limiting further movement of the flux tube radially outward near the LCFS. Comparisons with free boundary M3D-C1 simulations will be worth investigating.

Interestingly, we can repeat the procedure detailed above, but for a field line starting at the local minimum of the pressure perturbation near the outboard midplane at $\zeta = 0$. With this setup, we obtain an inwardly ballooned flux tube initially at $\rho = 0.83$ and displaced to $\rho = 0.72$, as shown in Fig. 9. Again, the constant p_{in} property holds approximately. A reasonable agreement between the flux tube shapes obtained from M3D-C1 and the nonlinear flux tube model with $\rho(\zeta = 0) = 0.68$ and $\rho_0 = 0.83$ is found.

4. Flux Tube Energy Calculation

In this section, we describe the general behavior of the change in energy due to displaced flux tubes and the subtleties of calculating this energy change in a numerical MHD equilibrium. First, we show the importance of choosing the right toroidal angle to integrate the change in the energy density of the flux tube. The Boozer toroidal angle is one of the possible right choices. Second, we show the error in the flux tube energy calculation caused by

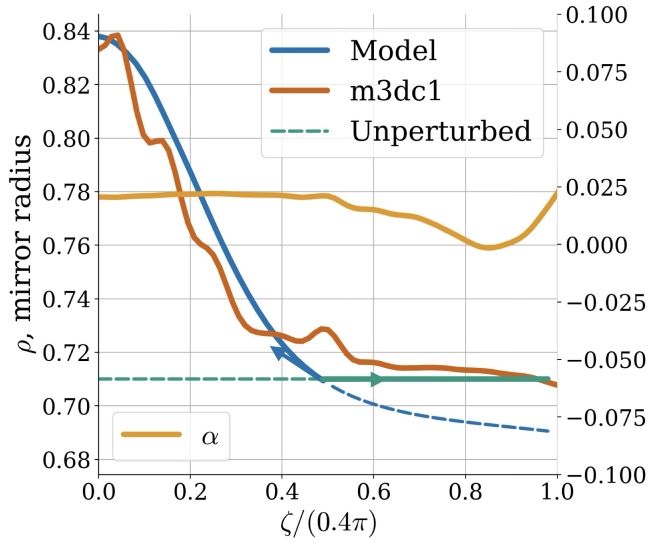


Figure 8: The flux tube shape extracted from the M3D-C1 simulation is compared with a flux tube obtained using the nonlinear ballooning flux tube model. The brown curve represents the flux tube extracted from the simulation by tracing the magnetic field line indicated in Fig.4. The blue curve is the solution to the nonlinear ballooning equation with $\rho(\zeta = 0) = 0.837$ and $\rho_0 = 0.71$ to match the pressure inside the flux tube. The yellow curve is the α_0 (i.e., $\theta - \iota\zeta$) value on the flux tube, with the value of α_0 given on the axis on the right.

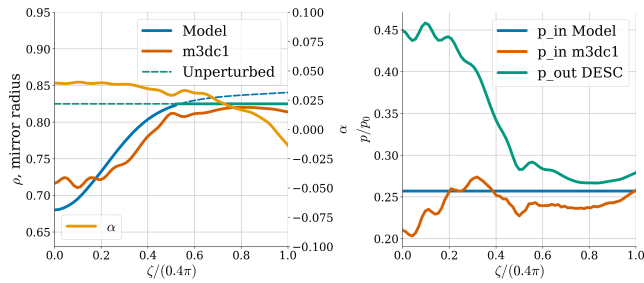


Figure 9: Inwardly ballooned flux tube. In the left panel, the brown curve represents the flux tube extracted from the simulation by tracing the magnetic field line starting at the local minimum of the pressure perturbation at $\zeta = 0$. The blue curve is the solution to the nonlinear ballooning equation with $\rho(\zeta = 0) = 0.68$ and $\rho_0 = 0.83$ to match the pressure inside the flux tube. In the right panel, the blue curve represents the pressure value inside the flux tube in our model. The brown curve is the the pressure value in M3D-C1 on the flux tube extracted from the simulation. The green curve is the pressure value in the DESC equilibrium on the flux tube extracted from the simulation, representing p_{out} in our model.

force errors in stellarator MHD equilibria are potentially very large. This makes the convergence of the energy change calculated by directly integrating Eq. 15 difficult. Finally, we introduced a variational approach to calculate the flux tube energy that overcomes the force error problem. Convergence on equilibrium resolution is demonstrated.

4.1. Energy Density and Choice of Toroidal Angle

Rewriting the energy functional (15) as an integral with respect to ζ , we have

$$\mathcal{E} = \int_{-\infty}^{+\infty} \left(B_{in}(\rho(\zeta), \zeta) \frac{dl}{d\zeta} - B_0(\rho_0, \zeta) \frac{dl_0}{d\zeta} \right) d\zeta \quad (16)$$

where l is the arc length of the field line, $d\zeta/dl = \mathbf{B}_{in} \cdot \nabla\zeta/B_{in}$ evaluated at $(\rho(\zeta), \zeta)$ and $d\zeta/dl_0 = \mathbf{B}_0 \cdot \nabla\zeta/B_0$ evaluated at (ρ_0, ζ) . The integrand of the energy functional (16) represents the energy density of a given flux tube element. If the integrand is plotted directly as a function of the cylindrical toroidal angle ζ , the energy has large oscillations even when the flux tube has wrapped around more than 10 toroidally turns, and the displaced flux tube approaches the unperturbed flux tube, as demonstrated by the blue dashed line in Fig.10. However, this does not mean that the part of the flux tube at large distance along its length contributes significantly to the energy. The large oscillations are due to the fact that we are not comparing with the right flux tube element of the unperturbed flux tube, as there is no reason that the perturbed flux tube element should have the same cylindrical toroidal angle as the original unperturbed flux tube element. Expanding the integrand assuming $(\rho(\zeta) - \rho_0)\zeta \rightarrow 0$, we have

$$B_{in}(\rho(\zeta), \zeta) \frac{dl}{d\zeta} \Big|_{\rho(\zeta), \zeta} - B_0(\rho_0, \zeta) \frac{dl}{d\zeta} \Big|_{\rho_0, \zeta} \sim B_0 \frac{dl}{d\zeta} \Big|_{\rho_0, \zeta, \theta = \iota_0\zeta + \iota'_0(\rho - \rho_0)\zeta} - B_0 \frac{dl}{d\zeta} \Big|_{\rho_0, \zeta, \theta = \iota_0\zeta} \quad (17)$$

Here the dominant contribution is the difference in energy of two neighboring flux tubes located at θ and $\theta + \iota'_0(\rho - \rho_0)\zeta$ because $\iota'_0(\rho - \rho_0)\zeta$ is much larger than $(\rho - \rho_0)$ when ζ is large. If $B_0 dl/d\zeta$ is dependent on θ , we will have oscillations in local energy density. Note that there will not be such contribution if we are doing calculations in a tokamak and we use θ as the coordinate along the flux tube instead of ζ because by holding θ constant, we are comparing flux tube pieces that are similar.

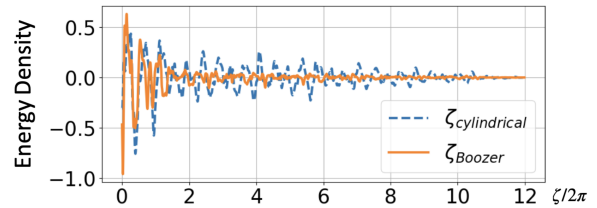


Figure 10: Energy density of a flux tube plotted against cylindrical toroidal angle versus Boozer toroidal angle

In order to have a physical energy density such that the contribution of flux tube displacement in θ vanishes, we should use the Boozer toroidal angle ζ_B , since $B_0 dl/d\zeta_B = B_0^2/\mathbf{B}_0 \cdot \nabla\zeta_B$ is a flux function, and not dependent on θ . As shown by the orange line in Fig.10, the energy density is now free from large oscillations at large distances along the flux tube.

4.2. Convergence Issue due to Numerical Equilibrium Force Error

In addition to the subtlety of having to choose the variable of integration, the consistent calculation of the flux tube energy is complicated by the numerical nature of stellarator MHD equilibria. A direct calculation of the energy of two saturated flux tubes by direct integration of Eq. 16 is presented as isolated triangular markers in Fig.11 (at this point the reader should ignore the continuous lines which will be explained in the later part of this section). The result does not match the physical picture obtained from flux tube displacement calculation and linear stability analysis. Linear ballooning stability analysis shows that the equilibrium is stable to linear ballooning modes at the minor radius of the unperturbed flux tube. This means that the unperturbed flux tube is on a local minimum of the energy. The equilibrium flux tube states with smaller displacement (corresponding to triangle markers near $\Delta\rho = 0.7$ in Fig.11) should be at a locally unstable equilibrium state. This means that the energy of the flux tube state with the smaller displacement should be larger than zero, but the energy of this state is below zero. Moreover, the calculated energy of the flux tubes does not converge with the size of the domain, even though the calculated flux tube displacement in ρ is converged. This mismatch comes from the force error in the numerical equilibrium. Unlike tokamak equilibria, which is proved to exist and numerically converges to zero force error, stellarator equilibria with integrable magnetic fields have not been proved to exist, and the numerical equilibria are not guaranteed to converge to zero force error.

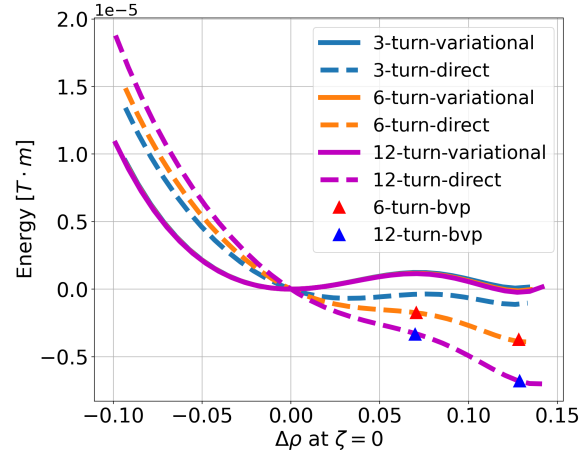


Figure 11: Comparison between the direct energy calculation and the variational method on a stellarator symmetric α surface on the compact QA equilibrium [25] with $\rho_0 = 0.85$. The horizontal axis is the displacement of the flux tube at $\zeta = 0$. Triangle markers indicate energy calculated directly for saturated flux tubes with different grid resolution and box size. Dashed curves shows the energy calculated directly for piecewise-equilibrium flux tubes with discontinuous slope at $\zeta = 0$. Solid curves show the energy calculated using the variational method for piecewise-equilibrium flux tubes with discontinuous slope at $\zeta = 0$. Cases with different simulation domain sizes in ζ are indicated by different colors (one turn equals 2π in ζ).

To illustrate the contribution of the force error, we compare the energy of two adjacent flux tubes by studying variations around a flux tube,

$$\delta\mathcal{E} = \int \delta\mathbf{r} \cdot [\mathbf{B}_0 \cdot \nabla\mathbf{B}_0 - \mathbf{B}_{in} \cdot \nabla\mathbf{B}_{in} + \mu_0(\nabla p - \mathbf{J} \times \mathbf{B})] \frac{dl}{B_{in}}. \quad (18)$$

For a detailed derivation, refer to Appendix B. We can apply formula (18) to the part of a saturated flux tube at large distances along the field line, where the displacement from the unperturbed flux tube is small and hence this variational formula gives the first order approximation to the energy contribution of this part of the flux tube. For an equilibrium flux tube, $\delta\mathbf{r} \cdot (\mathbf{B}_0 \cdot \nabla\mathbf{B}_0 - \mathbf{B}_{in} \cdot \nabla\mathbf{B}_{in}) = 0$, leading to

$$\delta\mathcal{E} = \int \frac{\delta\mathbf{r} \cdot \mathbf{F}_{err}}{B_{in}} dl, \quad (19)$$

where $\mathbf{F}_{err} = \mu_0(\nabla p - \mathbf{J} \times \mathbf{B})$ is the force error of the numerical MHD equilibrium. Expanding $\delta\mathbf{r}$ at small $\Delta\rho$, we find

$$\delta\mathbf{r} = \frac{\partial\mathbf{r}}{\partial\theta} l' \Delta\rho\zeta + \frac{\partial\mathbf{r}}{\partial\rho} \Delta\rho \quad (20)$$

The leading contribution as $\zeta \rightarrow \infty$ comes from the displacement in the θ direction due to finite magnetic

shear. As discussed in section 2, the saturated flux tube radial displacement behaves as $\Delta\rho \sim \zeta^\nu$ when $\zeta \gg 1$. For $-2 < \nu < -1$, the integral (19) does not converge in general. This is supported by the behavior of energy directly calculated when changing the simulation domain size in Fig. 11. The deviation grows with domain size while the flux tube displacement is almost unchanged.

4.3. Overcoming the Force Error Problem: a Variational Approach

To calculate an energy that converges with box size and to be consistent with the flux tube displacement behavior, we utilize the variational formula (18). First, to be able to perform a variational calculation, we allow the flux tube to be piece-wise C^1 and piece-wisely in equilibrium, that is, we allow a jump of derivative at a particular ζ , ζ_{cut} , as shown in Fig. 12. The sections on either side of the flux tube are in equilibrium, i.e. they satisfy Eqs. (6) and (14). With this discontinuity in slope, there is now a continuous family of piece-wise equilibrium flux tubes, labelled by the displacement $s = \Delta\rho_{cut}$ at ζ_{cut} . The flux tubes with continuous slope in this family are the flux tubes in force balance.

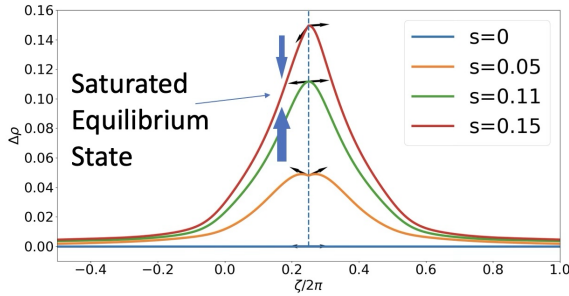


Figure 12: Shape of piece-wise C^1 flux tubes. Here, s is defined as the displacement $\Delta\rho$ at $\zeta = \zeta_{cut}$. Saturated states have no discontinuity in slope, as exemplified by the green curve with $s = 0.11$. Out of equilibrium flux tubes $s = 0.05$ and $s = 0.15$ have a discontinuity in the slope. The magnetic tension force due to the slope discontinuity points towards the saturated state. Calculated from a finite β ESTELL equilibrium with a non-stellarator symmetric α surface and $\rho_0 = 0.85$.

We use an updated version of the variational formula that takes discontinuity of slope into account (derived in Appendix B, Eq. (B.7)),

$$\delta\mathcal{E} = \int_{-\infty}^{+\infty} \frac{1}{B_{in}} (\mathbf{B}_0 \cdot \nabla \mathbf{B}_0 - \mathbf{B}_{in} \cdot \nabla \mathbf{B}_{in} + \mathbf{F}_{err}) \cdot \delta \mathbf{r} dl - [\mathbf{B}_{in}]_{cut} \cdot \delta \mathbf{r}_{cut}. \quad (21)$$

Here $[A]$ denotes the jump of quantity A across $\zeta = \zeta_{cut}$. The variation $\delta \mathbf{r}$ is a continuous vector function of l . The contribution from the force error (the first term) and the rest (the second term) can now be separated. The part that is independent of force error can be calculated by

integrating $[\mathbf{B}_{in}] \cdot \frac{\delta \mathbf{r}_{cut}}{\delta s}$ in displacement s . It can be readily seen that the energy calculated in this way is consistent with the behavior of flux tube displacement: since $[\mathbf{B}_{in}]$ is zero for equilibrium flux tubes, they are automatically the stationary point of the energy curve. With this method, the procedure for calculating the energy of an equilibrium flux tube is as follows. First, a family of flux tubes is obtained by integrating from the two ends of the simulation domain to where the cut is. All the flux tubes have zero radial displacement at the ends of the domain by construction. Each flux tube ends at a different radial location at the ζ cut. Note that it is not necessary that flux tubes calculated in this way join at the cut unless the ζ_{cut} is chosen to be at a symmetry point. With the family of flux tubes calculated in this way, \mathbf{B}_{in} on both sides of the cut can be interpolated as a function of radial displacement at the cut, and then $[\mathbf{B}_{in}]$ can be integrated to calculate the energy of each piece-wise equilibrium flux tube. The stationary point of the energy curve correspond to the energy and displacement of the equilibrium flux tubes. We can also get the shape of the equilibrium flux tubes by interpolating the family of the piece-wise equilibrium flux tubes as a 2D function $\Delta\rho(\zeta, s)$, where the radial displacement at the cut s works as a flux tube label. The equilibrium flux tubes shape are $\Delta\rho(\zeta, s_{eq})$, where s_{eq} are the radial displacement at the cut that correspond to a stationary point on the energy curve.

This method is effectively a nonlinear extension of Newcomb's principle [28]. In the linear limit, if the solution crosses zero, we can truncate the solution at the intersection and join it with the unperturbed flux tube. Using the argument of field line tension described in Fig.12, the flux tube tends to move upwards at the cross-over location, i.e. it is unstable.

As a side note, using the shooting method to find the saturated flux tubes, described in section 2, requires first mapping out the flux tube behavior by varying the slope at one end. This generates a curve of $\Delta\rho(\zeta = \zeta_1)$ v.s. $Y(\zeta_0)$. The interval to find the correct Y is the one that includes the value of $Y(\zeta_0)$ where $\Delta\rho(\zeta = \zeta_1)$ crosses zero. Once the bounds of the slope are obtained, a root finding algorithm is used. Compared with the variational approach, the shooting method requires a coarser scan of the slopes, but the second root finding step requires additional ODE IVP solves and it is serial. Instead, the variational approach can be easily parallelized. It also generates the energy value using the discontinuity in slope at the cut. The variational approach is typically more computational advantageous.

We plot the energy of a family of flux tubes as a function of s in Fig. 11. The energy curves are insensitive to the simulation domain size. The dashed lines are the energy curves calculated for the family of piece-wise equilibrium flux tubes using Eq. (16). The difference between the two sets of curves is the contribution from the equilibrium force error. This contribution is significant, especially near marginality where the energy is small.

To further illustrate the problem with the equilibrium force error, we confirm in Fig. 13 that in a tokamak equilibrium, where the force error is three orders of magnitude lower than that in the compact QA case [25] that we are using, the two ways of calculating the energy match each other.

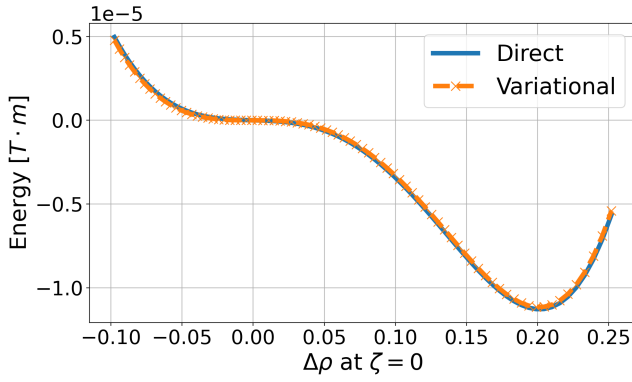


Figure 13: Comparison between the piecewise C^1 flux tube energy calculated using the variational method and the same energy calculated using the direct method in a tokamak equilibrium (The DSHAPE Case in [24]). The α surface is up-down symmetric on the outboard mid-plane. The simulation domain is $\zeta \in [0, 24\pi]$. The relative force error $F_{error}/|\nabla B^2|$ is smaller than 10^{-6} in this equilibrium.

Given that the cut location is arbitrary, the energy of the saturated flux tubes should be independent of this choice. This is demonstrated by Fig. 14, which illustrates that the stationary points of all energy curves generated with differing cut locations coincide.

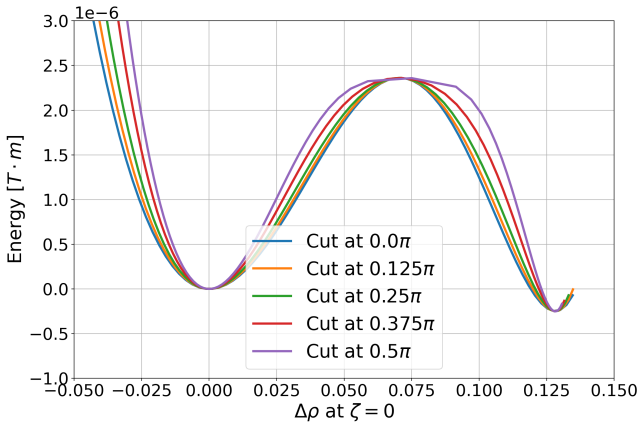


Figure 14: Energy of nonlinearly saturated flux tubes in a compact QA equilibrium [25] calculated using the variational method with different location of the slope discontinuity ζ_{cut} . The horizontal axis is the displacement of the flux tubes at $\zeta = 0$. The local maximum and minimum of energy curve correspond to the saturated flux tube state. They remain unchanged when ζ_{cut} varies.

We have found that the nonlinear ballooning saturation calculation is convergent with respect to numerical choice in the solver and **box size**. In Fig. 15 we demonstrate the convergence with respect to numerical equilibrium resolution. We generated four equilibria with increasing resolution for an ESTELL fixed boundary equilibrium [29]. Due

to the nature of the variational calculation method, the energy of a flux tube converges as long as the flux tube shape calculation converges.

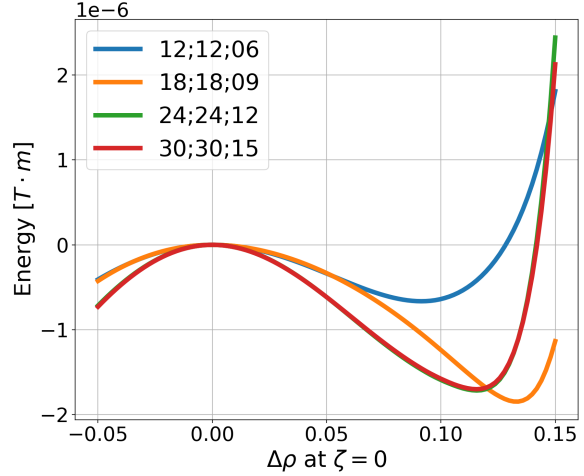


Figure 15: Convergence of flux tube energy curves, calculated using the variational method, for the same unperturbed flux tube with different equilibrium resolution. The equilibrium resolution is labelled by a tuple of three integers, each representing radial mode number, poloidal mode number and toroidal mode number. The equilibrium is for a finite beta version of ESTELL at $\rho_0 = 0.85$.

One thing to note is that, similar to linear ballooning calculations, the nonlinear ballooning calculation is sensitive to small changes in equilibrium. A correct calculation usually requires a high resolution for the numerical equilibrium and a careful convergence analysis. As a rule of thumb, the nonlinear results is usually correct when the linear ballooning growth rate converges in the entire domain of the nonlinear calculation (which also indicates convergence of the Mercier stability calculation).

We have found stellarator equilibria whose nonlinear ballooning calculation does not converge with increasing equilibria resolution to the level of resolution that we could afford. However, in those cases, their linear ballooning growth rate did not converge either. The study of this lack of convergence is out of the scope of this paper.

5. Case study on a compact QA [25] equilibrium

In this section we study the behavior of nonlinear saturated flux tubes in compact QA equilibria [25]. First we will show that in the standard configuration of [25], stable, unstable and metastable magnetic flux tubes exist. Then, we construct a modified equilibrium with slightly lower β , just below the linear instability boundary, and we show that in this globally linearly stable case, metastable flux tubes exist.

We follow the following procedure for each equilibrium. For each equilibrium configuration, linear stability is analyzed near the stellarator last closed flux surface (LCFS). Then, for each radial location, the nonlinear ballooning equation is solved on the stellarator symmetric α surface centered at $\theta = 0, \zeta = 0$ to find saturated flux tubes that do not balloon outside the LCFS. For each saturated flux tube, we also calculate the energy (Eq. (15)). We have chosen the α surfaces to be stellarator symmetric because in most flux surfaces, the most unstable modes are symmetric with respect to $\zeta = 0, \theta = 0$.

5.1. Standard Configuration with Linear Ballooning Instability

In Fig. 16, the maximum radial displacement along the saturated flux tube is plotted as a function of the radial location of the corresponding unperturbed flux tube, for the compact QA [25] standard configuration. There are two different branches of saturated flux tubes, each corresponding to a stationary point on the energy curve, as indicated by the energy curve in the subfigure in Fig. 16. On top of the displacement, the linear ballooning growth rate is also plotted for reference. As indicated, there is a linear unstable region from minor radius $\rho = 0.85$ to 0.95. Some typical saturated flux tubes of the second branch (orange colored) are plotted in Fig. 17. Note that the y axis in Fig. 17 is the minor radius ρ instead of the radial displacement $\Delta\rho$ and therefore different saturated flux tubes go back to different ρ_0 , their unperturbed location.

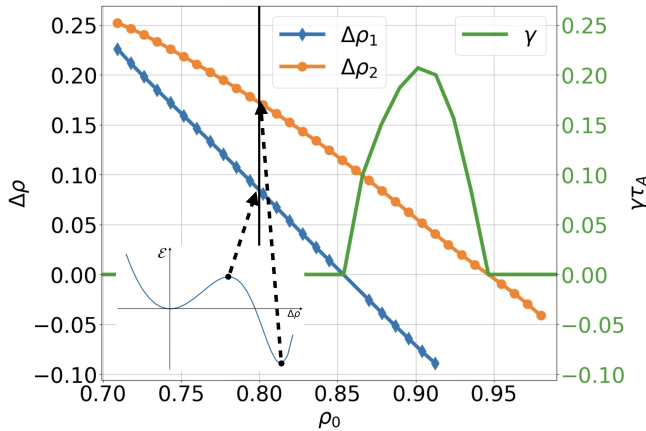


Figure 16: Saturated flux tube maximum displacement calculated on a compact QA [25] equilibrium. Here, $\Delta\rho$ denotes the displacement of the flux tube at $\zeta = 0$, and ρ_0 denotes the flux surface label of the original, unperturbed flux tube. We also plot the normalized (to Alfvén frequency) linear ballooning growth rate γ (values given on the right). The corresponding energy curve of the flux tube initially at $\rho = 0.8$ is shown on the lower left corner. The two branches correspond to two stationary points of the energy curve as indicated.

In Fig. 18, the energy of the flux tubes in Fig. 16 is plotted. As we can see, the nonlinear saturated flux tubes

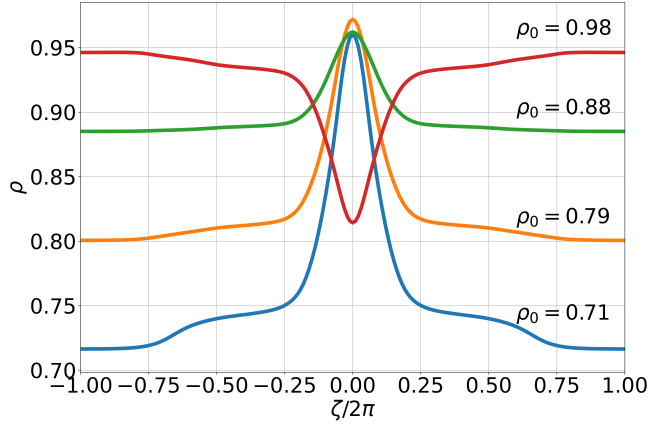


Figure 17: Saturated flux tube shape on the compact QA equilibrium [25]. The y axis is the minor radius ρ instead of displacement $\Delta\rho$. Note that for the $\rho_0 = 0.98$ case, the $\Delta\rho_1$ branch of Fig. 16 is plotted since it has a lower energy. For the rest of the cases, the $\Delta\rho_2$ branch has lower energy and are plotted.

exist from minor radius $\rho_0 = 0.7$ all the way to the LCFS. For $\rho_0 \in (0.7, 0.77)$, both branches of the saturated flux tubes $\Delta\rho_1$ and $\Delta\rho_2$ have higher energy than the original flux tube, making the plasma nonlinearly stable to localized perturbations in this region. For $\rho_0 \in (0.77, 0.85)$, the branch $\Delta\rho_2$ of the saturated flux tubes has lower energy than the original flux tube, whereas the branch $\Delta\rho_1$ still has higher energy than the original flux tube. In this region, flux tubes are metastable, with a maximum displacement of 15% of the minor radius. In both of these regions, the saturated flux tubes in branch $\Delta\rho_1$ correspond to local maxima of the energy curve. The flux tubes on the branch $\Delta\rho_1$ are hence unstable and in reality only branch $\Delta\rho_2$ of the saturated flux tubes or the unperturbed flux tubes can exist. For $\rho_0 \in (0.85, 0.95)$, the ballooning mode becomes linearly unstable as indicated by the non-zero linear growth rate. Both branches of the perturbed flux tubes have lower energy and the nonlinear theory predicts their saturation levels. One of the branches balloons radially inwards, and the other branch balloons radially outwards, which is expected since the leading order term of the energy functional is quadratic in amplitude. In the region close to marginality, one of the two branches of the saturated flux tube should have small saturated level and small energy release, and go to zero at the marginally stable surface. This is indeed the case in the nonlinear calculation, where the saturated flux tube displacement and energy curves go to zero exactly where linear growth rate goes to zero.

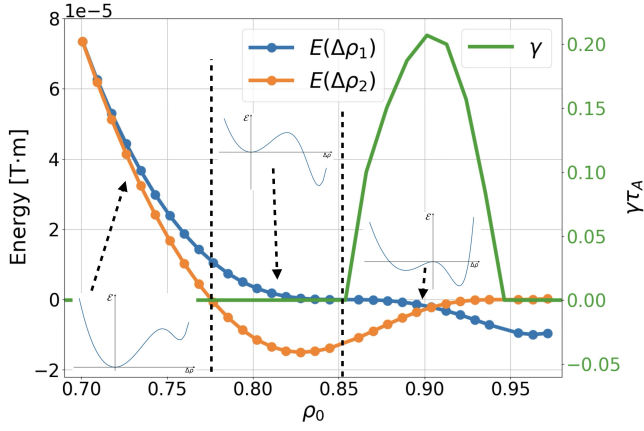


Figure 18: Saturated flux tube energy calculated on the compact QA [25] equilibrium. Here, ρ_0 denotes the flux surface label of the original, unperturbed flux tube. We also plot the normalized linear ballooning growth rate γ (see values on the right).

In the compact QA [25] standard configuration, nonlinearly stable, metastable and linearly unstable flux tubes exist in different minor radii.

5.2. Modified Linearly Stable Configuration: Metastability

We scale down the pressure profile in the standard configuration by 3% so that the new configuration is linearly stable to ballooning modes everywhere (at worst marginally stable) and perform the same nonlinear ballooning analysis procedure used above. The nonlinear saturated flux tube displacement and energy are plotted in Figs. 19, 21 and 20.

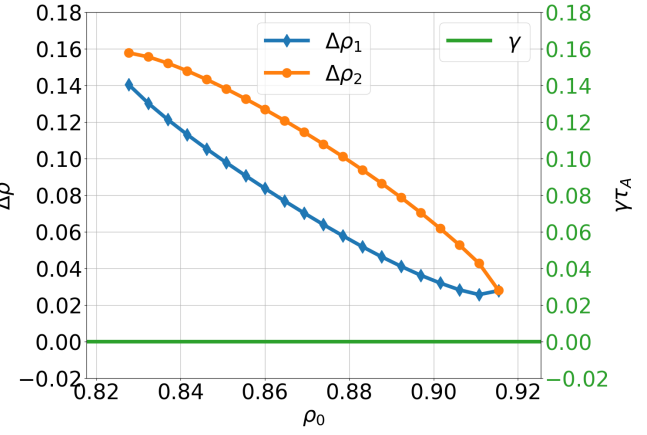


Figure 19: Saturated flux tube maximum displacement calculated in the compact QA equilibrium [25] with scaled pressure profile. Here, $\Delta\rho$ denotes the displacement of the flux tube at $\zeta = 0$, ρ_0 denotes the flux surface label of the original, unperturbed flux tube. We also plot the normalized linear ballooning growth rate γ (see values on the right), indicating that this α surface is globally stable.

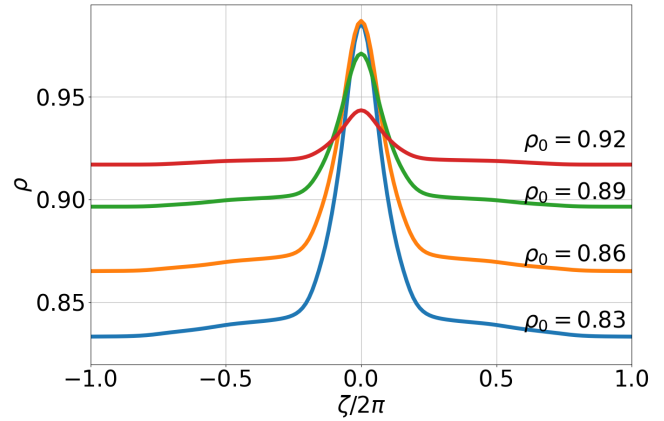


Figure 20: Saturated flux tube shape on the compact QA equilibrium [25] for branch $\Delta\rho_2$ in Fig. 19. The y axis is the minor radius ρ instead of displacement $\Delta\rho$.

At $\rho_0 = 0.89$, we can see that despite the equilibrium being linearly stable across the entire minor radius, there still exist metastable flux tubes. Note that the energy release is small compared to the metastable flux tubes in the standard compact QA equilibrium [25]. However, this is expected to be sensitive to how close the equilibrium is to marginality and the radial extent of the marginally stable region [1].

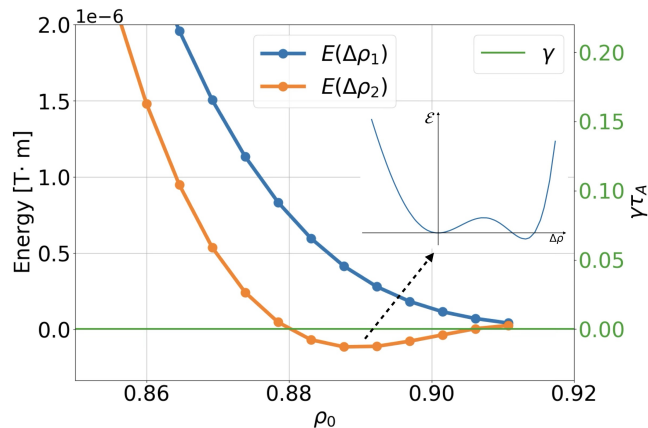


Figure 21: Saturated flux tube energy calculated on the compact QA [25] equilibrium. Here, ρ_0 denotes the flux surface label of the original, unperturbed flux tube. We also plot the normalized linear ballooning growth rate γ (values on the right). The arrow points to the energy curve for the piecewise C^1 flux tubes calculated for $\rho_0 = 0.885$, showing the existence of metastable state.

6. Conclusions

We have developed a set of novel tools to calculate the nonlinear saturation of ballooning modes in stellarators using the model in [1] and the DESC equilibrium solver [24]. Convergence analysis and benchmarks against linear ballooning codes have been performed. A variational method for flux tube energy calculation was developed to eliminate the contribution due to the finite force error in the stellarator numerical equilibrium. This contribution impeded the convergence of the direct way of calculating energy.

By analyzing a recent simulation of W7X using M3D-C1 [23], we show that nonlinear saturated flux tube structures like the ones proposed in [1] and in this article exist in a global nonlinear MHD simulation. In the nonlinear saturated stage, the pressure perturbation has localized peaks in a toroidal cross-section. These peaks of the pressure perturbation roughly follow field lines, thus resembling the flux tube in [1]. The shape of the pressure perturbation contour near the peak is elongated along an α surface. Total pressure balance across the α surface and hydrodynamic pressure balance along the flux tube were each checked to hold approximately. We have compared the flux tube displacement extracted from the simulation with our nonlinear ballooning model, finding good agreement.

A study of modified compact QA equilibria [25] shows the existence of stable, unstable and metastable flux tubes. When the equilibrium is linearly stable globally but close to marginal stability, lower energy states can also be found, thus the unperturbed equilibrium is metastable. This indicates that explosive MHD behavior can also happen in stellarator. The existence of such metastable flux tube states might be related to ELM-like bursts observed in stellarators [3].

One thing to note here is that the calculation of the nonlinear saturated state is very sensitive to the numerical equilibrium. This behavior is also observed in linear ballooning growth rate calculations. Careful convergence studies of the equilibrium resolutions need to be conducted for each calculation. The results might not converge for some highly shape equilibria, for which the required resolution is not attainable with the computation power that we had. A general rule of thumb is that the nonlinear ballooning calculation is convergent as long as the linear ballooning growth rate calculation has converged for each field line on each flux surface. Further studies on which part of the equilibrium lead to this sensitivity and how to reduce such sensitivity are needed.

Compared with tokamaks, no qualitative difference in the existence and behavior of nonlinear saturated flux tube states has been observed so far. Near marginal stability, the second order terms in the energy principle approach zero. As long as there is a non-zero third order term, metastable equilibria generally exist. This can be backed up by the fact that we found metastable equilibria in our case study and no special changes of the magnetic geometry were introduced to find them. Lower energy saturated states even exist in configurations that are linearly stable over the whole volume. The energy release is small in the metastable cases we presented, but this is expected to be configuration dependent. From empirical experience with this model on tokamaks, increasing the radial extent of marginal stable region generally increases the energy release of the metastable flux tubes [1].

Acknowledgements

The authors would like to thank Dario Panici and Rahul Gaur for the DESC code support. This work is supported by the U.S. Department of Energy under contract number DE-AC02-09CH11466. Y.Z. is supported by the National MCF R&D Program under Grant Number 2024YFE03230400 and the Fundamental Research Funds for the Central Universities. The United States Government retains a non-exclusive, paid-up, irrevocable, world-wide license to publish or reproduce the published form of this manuscript, or allow others to do so, for United States Government purposes.

- [1] Ham C J, Cowley S C, Brochard G *et al.* 2018 *Plasma Physics and Controlled Fusion* **60** 075017 ISSN 0741-3335 publisher: IOP Publishing
- [2] Ham C, Cowley S, Brochard G *et al.* 2016 *Physical Review Letters* **116** 235001 publisher: American Physical Society
- [3] Hirsch M, Baldzuhn J, Beidler C *et al.* 2008 *Plasma Physics and Controlled Fusion* **50** 053001 ISSN 0741-3335, 1361-6587
- [4] Sakakibara S, Watanabe K Y, Suzuki Y *et al.* 2008 *Plasma Physics and Controlled Fusion* **50** 124014 ISSN 0741-3335, 1361-6587
- [5] Klinger T, Andreeva T, Bozhnikov S *et al.* 2019 *Nuclear Fusion* **59** 112004 ISSN 0029-5515, 1741-4326
- [6] Weller A, Sakakibara S, Watanabe K Y *et al.* 2006 *Fusion Science and Technology* **50** 158–170 ISSN 1536-1055, 1943-7641
- [7] Leonard A W 2014 *Physics of Plasmas* **21** 090501 ISSN 1070-664X

- [8] Connor J W, Hastie R J and Taylor J B 1979 *Proceedings of the Royal Society of London. A. Mathematical and Physical Sciences* **365** 1–17 publisher: Royal Society
- [9] Geiger J E, Weller A, Zarnstorff M C *et al.* 2004 *Fusion Science and Technology* **46** 13–23 ISSN 1536-1055, 1943-7641
- [10] Ohdachi S, Watanabe K, Tanaka K *et al.* 2017 *Nuclear Fusion* **57** 066042 ISSN 0029-5515, 1741-4326
- [11] Connor J W, Hastie R J and Taylor J B 1978 *Physical Review Letters* **40** 396–399 ISSN 0031-9007
- [12] Greene J M and Chance M S 1981 *Nuclear Fusion* **21** 453 ISSN 0029-5515
- [13] Dewar R L and Glasser A H 1983 *Physics of Fluids* **26** 3038
- [14] Hegna C C and Nakajima N 1998 *Physics of Plasmas* **5** 1336–1344 ISSN 1070-664X
- [15] Sanchez R, Hirshman S P, Ware A S *et al.* 2000 *Plasma Physics and Controlled Fusion* **42** 641–653 ISSN 0741-3335, 1361-6587
- [16] Miller R L and Dam J W V 1987 *Nuclear Fusion* **27** 2101 ISSN 0029-5515
- [17] Anderson D, Cooper W, Gruber R *et al.* 1990 *The International Journal of Supercomputing Applications* **4** 34–47 ISSN 0890-2720
- [18] Cowley S C and Artun M 1997 *Physics Reports* **283** 185–211 ISSN 0370-1573
- [19] Hurricane O A, Fong B H and Cowley S C 1997 *Physics of Plasmas* **4** 3565–3580 ISSN 1070-664X
- [20] Henneberg S A, Cowley S C and Wilson H R 2015 *Plasma Physics and Controlled Fusion* **57** 125010 ISSN 0741-3335 publisher: IOP Publishing
- [21] Zhu P and Hegna C C 2008 *Physics of Plasmas* **15** 092306 ISSN 1070-664X
- [22] Zhou Y, Ferraro N, Jardin S *et al.* 2021 *Nuclear Fusion* **61** 086015 ISSN 0029-5515, 1741-4326
- [23] Zhou Y, Aleynikova K, Liu C *et al.* 2024 *Physical Review Letters* **133** 135102 ISSN 0031-9007, 1079-7114
- [24] Panici D, Conlin R, Dudt D W *et al.* 2023 *Journal of Plasma Physics* **89** 955890303 ISSN 0022-3778, 1469-7807
- [25] Nelson B, Berry L, Brooks A *et al.* 2002 Design of the National Compact Stellarator Experiment (NCSX) core *Proceedings of the 19th IEEE/IPSS Symposium on Fusion Engineering. 19th SOFE (Cat. No.02CH37231)* (Atlantic City, NJ, USA: IEEE) pp 285–289 ISBN 978-0-7803-7073-9
- [26] 1972 Algorithms for Minimization without Derivatives *Algorithms for minimization without derivatives* Prentice-Hall series in automatic computation (Englewood Cliffs, N.J: Prentice-Hall) pp Ch. 3–4 ISBN 978-0-13-022335-7
- [27] Cowley S C, Cowley B, Henneberg S A *et al.* 2015 *Proceedings of the Royal Society A: Mathematical, Physical and Engineering Sciences* **471** 20140913 publisher: Royal Society
- [28] Newcomb W A 1960 *Annals of Physics* **10** 232–267 ISSN 00034916
- [29] Drevlak M, Brochard F, Helander P *et al.* 2013 *Contributions to Plasma Physics* **53** 459–468 ISSN 0863-1042, 1521-3986
- [30] Connor J W and Taylor J B 1987 *The Physics of Fluids* **30** 3180–3185 ISSN 0031-9171 publisher: AIP Publishing

Appendix A. Numerical implementation of the nonlinear ballooning equations (6) and (14)

Initially, the computational domain, namely the α surface, is set up. We construct a 2D uniform grid in ζ_{DESC} and ρ on the α surface. The alpha surface is defined by

$$\alpha = \theta_{DESC} + \lambda_{DESC} - \iota\zeta_{DESC} - f(\rho), \quad (\text{A.1})$$

where f is a prescribed function, such as a polynomial. Here, ζ_{DESC} is the toroidal angle used in DESC, which is the same as the cylindrical toroidal angle, θ_{DESC} is the poloidal angle used in DESC, and λ_{DESC} is the difference between the straight field line poloidal angle corresponding to ζ_{DESC} and θ_{DESC} . On the grid points, equilibrium quantities required to calculate the RHS of Eq.(6) and Eq.(14) given ζ and Y are calculated and interpolated using cubic splines.

After the setup stage, Eqs. (6) and (14) are solved using the RK45 integrator given initial condition for η and Y . To find a saturated state, two methods can be used. One option is a shooting method that seeks flux tubes that satisfy $\eta(\zeta_0) = \eta(\zeta_1) = 0$ at the boundary of the simulation box. Brent's method [26] is used to find the value of Y_0 that gives $\eta(\zeta_1) = 0$, where Y_0 is Y at $\zeta = \zeta_0$. The other method utilizes the piecewise C^1 equilibrium flux tubes introduced in section 4. A series of flux tubes is calculated starting with different Y_0 at both ends of the simulation domain and ending at a preset $\zeta = \zeta_{cut}$ in the middle. On both sides of ζ_{cut} , the solutions is interpolated as a function of Y_0 and ζ , $\eta(\zeta, Y_0)$. When Y_0 is fixed and ζ varied, $\eta(\zeta, Y_0)$ is a solution to Eq.(6) and Eq.(14) with initial condition $Y = Y_0$. The equilibrium flux tube is found when $\partial_\zeta \eta(\zeta_{cut}^-, Y_0) = \partial_\zeta \eta(\zeta_{cut}^+, Y_0)$ with the piecewise C^1 solutions. The energy of the flux tube can be calculated by the variational approach introduced in section 4.

Appendix B. Variational derivation of Eq.(12)

We want to minimize the functional in Eq. (15) with the constraint that the variation stays on the α surface

$$\delta \mathbf{r} \cdot \nabla \alpha = 0. \quad (\text{B.1})$$

With this constraint, we have

$$\delta \mathbf{r} = \delta r_1 \mathbf{b}_{in} + \delta r_2 \mathbf{e}_\perp \quad (\text{B.2})$$

where δr_1 and δr_2 are scalars and $\mathbf{b}_{in} = \mathbf{B}_{in}/|\mathbf{B}_{in}|$ is the unit vector parallel to the displaced flux tube. The displacement $\delta \mathbf{r}$ should be a continuous function of l .

The change in the energy functional due to the displacement $\delta \mathbf{r}$, after integrating by part, is

$$\begin{aligned} \delta \mathcal{E} = & \int_{l_0}^{l_1} \delta \mathbf{r} \cdot (\nabla B_{in} - B_{in} \mathbf{b}_{in} \cdot \nabla \mathbf{b}_{in} - \mathbf{b}_{in} (\mathbf{b}_{in} \cdot \nabla B_{in})) dl \\ & + (\mathbf{B}_{in} \cdot \delta \mathbf{r})|_0^1. \end{aligned} \quad (\text{B.3})$$

For a smooth perturbed flux tube that goes to zero at $-\infty$ and $+\infty$, Eqs. (B.2) and (B.3) gives

$$\mathbf{b}_{in} \cdot (\nabla B_{in} - B_{in} \mathbf{b}_{in} \cdot \nabla \mathbf{b}_{in} - \mathbf{b}_{in} (\mathbf{b}_{in} \cdot \nabla B_{in})) = 0, \quad (\text{B.4})$$

and

$$\mathbf{e}_\perp \cdot (\nabla B_{in} - B_{in} \mathbf{b}_{in} \cdot \nabla \mathbf{b}_{in} - \mathbf{b}_{in} (\mathbf{b}_{in} \cdot \nabla B_{in})) = 0. \quad (\text{B.5})$$

Eq. (B.4) is automatically satisfied. Eq. (B.5) gives Eq. (12) after some manipulations. Indeed, Using Eq. (7),

we find

$$\begin{aligned}
 & B_{in} [\nabla B_{in} - B_{in} \mathbf{b}_{in} \cdot \nabla \mathbf{b}_{in} - \mathbf{b}_{in} (\mathbf{b}_{in} \cdot \nabla B_{in})] \\
 &= \nabla (B_0^2/2 + \mu_0 p) - \mathbf{B}_{in} \cdot \nabla \mathbf{B}_{in} \\
 &= \mathbf{B}_0 \cdot \nabla \mathbf{B}_0 - \mathbf{B}_{in} \cdot \nabla \mathbf{B}_{in} + (\mu_0 \nabla p - \mathbf{J} \times \mathbf{B}). \quad (\text{B.6})
 \end{aligned}$$

Therefore, for a numerical equilibrium where $\mu_0 \nabla p - \mathbf{J} \times \mathbf{B} \neq 0$, there will be a mismatch between the solution of the flux tube equilibrium solution and the stationary point of the energy functional.

For section 4, it is useful to consider a perturbed flux tube that goes to zero at $-\infty$ and $+\infty$ but has a discontinuity of slope at a location l_{cut} . The change of energy due to a displacement $\delta \mathbf{r}$ of such a flux tube is

$$\begin{aligned}
 \delta \mathcal{E} &= \int_{-\infty}^{l_{cut}} \delta \mathbf{r} \cdot (\nabla B_{in} - B_{in} \mathbf{b}_{in} \cdot \nabla \mathbf{b}_{in} - \mathbf{b}_{in} (\mathbf{b}_{in} \cdot \nabla B_{in})) dl \\
 &+ \int_{l_{cut}}^{+\infty} \delta \mathbf{r} \cdot (\nabla B_{in} - B_{in} \mathbf{b}_{in} \cdot \nabla \mathbf{b}_{in} - \mathbf{b}_{in} (\mathbf{b}_{in} \cdot \nabla B_{in})) dl \\
 &- [\mathbf{B}_{in}]_{l_{cut}} \cdot \delta \mathbf{r}|_{l_{cut}} = - [\mathbf{B}_{in}]_{l_{cut}} \cdot \delta \mathbf{r}|_{l_{cut}}. \quad (\text{B.7})
 \end{aligned}$$

The last equality holds when the flux tube pieces on both sides of the discontinuity are in equilibrium.

Appendix C. Behavior of the displaced flux tube at large ζ

In this appendix, we calculate the behavior of the nonlinear ballooning equation at large ζ by performing a two-scale expansion of the full nonlinear ballooning equation (12). We need a two-scale expansion because the coefficient in Eq. (12) have two different dependence on ζ : some of them oscillate and some of them change secularly with ζ . The particular term that increase secularly is $|\mathbf{e}_\perp|$, which can be conveniently expressed as

$$|\mathbf{e}_\perp|^2 = |\nabla \psi|^2 L_a^2 + \frac{B_0^2}{|\nabla \psi|^2}. \quad (\text{C.1})$$

Here $L_a = \iota'(\eta) \zeta - h(\eta, \zeta)$ and

$$h = \frac{(\nabla \theta - \iota \nabla \zeta) \cdot \nabla \psi}{|\nabla \psi|^2}. \quad (\text{C.2})$$

When ζ is large ($\eta \rightarrow 0$), L_a can be approximated by L , which is defined as

$$L = \iota'|_0 \zeta - h|_0(\zeta). \quad (\text{C.3})$$

The subscript $|_0$ indicates that the function is evaluated on an approximation to the α surface, with the coordinates given by ρ_0 , ζ and $\theta = f(\rho_0) + \iota(\rho_0)\zeta + \iota'(\rho_0)\eta(\zeta)\zeta$.

Since $|\mathbf{e}_\perp|$ can be approximated by $L|\nabla \psi|$ at large L , we find it convenient to use the two scale expansion for η

$$\eta = L^{-\gamma} (\eta_0(\zeta) + \eta_1(\zeta)L^{-1} + \eta_2(\zeta)L^{-2} \dots). \quad (\text{C.4})$$

Here the functions η_i with $i \geq 0$, represent the fast variation of η with ζ , and L is the slow scale along the field line. We assume $L \gg 1$. Note that for $\gamma \leq 1$, the displaced flux tube does not converge to the original flux tube because $\theta \sim \iota' \eta \zeta$ for large ζ . Thus from here on we assume $\gamma > 1$.

For $\gamma > 1$ and $L \gg 1$, $\eta \sim L^{-\gamma}$ and $d\eta/d\zeta \sim d\eta_0/d\zeta L^{-\gamma} + \eta_0 L^{-\gamma-1}$. Therefore, the derivative of η with respect to ζ tends to zero even when multiplied by the large coordinate L , $L d\eta/d\zeta \sim O(L^{1-\gamma}) \ll 1$. This means that $|\mathbf{e}_\perp B_\perp|$ tends to zero as $L \rightarrow \infty$ and $B_\perp \simeq (\mathbf{B}_0 \cdot \nabla \zeta / B_0) d\eta/d\zeta$ to leading order in L . Using this fact, we can estimate the leading order behavior of different terms in the nonlinear ballooning equation. The field line bending term $\mathbf{B}_{in} \cdot \nabla [(|\mathbf{e}_\perp|^2 / B_0) B_\perp]$ is $O(L^2 d\eta/d\zeta) \sim O(L^{2-\gamma})$, the instability drive term $(B_\parallel^2 - 1) B_0 \boldsymbol{\kappa} \cdot \mathbf{e}_\perp$ is $O(\max(L^{1-\gamma} \eta_0, L^3 (d\eta/d\zeta)^2))$ and the nonlinear local shear term $B_\perp^2 B_0 \mathbf{e}_\perp \cdot \nabla (|\mathbf{e}_\perp|^2 / 2 B_0^2)$ is $O(L^3 (d\eta/d\zeta)^2)$. The leading order term among all the three terms is the linear field line bending term, which consists of only fast scale derivatives of η_0

$$\frac{d}{d\zeta} \frac{|\nabla \psi|^2}{B_0^2} \frac{d\eta_0}{d\zeta} = 0 \quad (\text{C.5})$$

This equation has a solution of the form of $d\eta_0/d\zeta = B_0^2 C / |\nabla \psi|^2$, where C is a constant of integration. For η_0 not to change secularly with ζ , $B_0^2 C / |\nabla \psi|^2$ needs to average to zero after several toroidal turns. This is only possible if $C = 0$, and hence we have $d\eta_0/d\zeta = 0$.

The result $d\eta_0/d\zeta = 0$ means that we have $d\eta/d\zeta \sim O(L^{-\gamma-1})$. The nonlinear local shear term $B_\perp^2 B_0 \mathbf{e}_\perp \cdot \nabla (|\mathbf{e}_\perp|^2 / 2 B_0^2)$ is $O(L^{1-2\gamma}) \ll O(L^{-\gamma})$. One can also show that the leading order nonlinear contribution in both the field line bending term $\mathbf{B}_{in} \cdot \nabla [(|\mathbf{e}_\perp|^2 / B_0) B_\perp]$ and the instability drive term $(B_\parallel^2 - 1) B_0 \boldsymbol{\kappa} \cdot \mathbf{e}_\perp$ are $O(L^{1-2\gamma})$ or smaller. Therefore, the contributions $O(L^{1-\gamma})$ and $O(L^{-\gamma})$ are all from linear terms. This leads to the same results that one obtains expanding the linear ballooning equation at large ζ (see [30]) and hence predicts same γ . This is the γ provided by Mercier analysis.

To summarize, even for the fully nonlinear ballooning equation, the behavior of the displaced flux tube is predicted by the exponent γ from the Mercier analysis of the linear ballooning equation when $\gamma > 1$. As we explained above, the solutions for $\gamma \geq 1$ are not physical.